Dynamic Stereochemical Activity of the Sn^{2+} Lone Pair in Perovskite CsSnBr$_3$

Douglas H. Fabini,[†,‡,#] Geneva Laurita,[†,#] Jonathon S. Bechtel,[†,‡] Constantinos C. Stoumpos,[¶] Hayden A. Evans,[†,§] Athanassios G. Kontos,[∥] Yannis S. Raptis,[⊥] Polycarpos Falaras,[∥] Anton Van der Ven,[†,‡] Mercouri G. Kanatzidis,[¶] and Ram Seshadri*,[†,‡,§]

[†]Materials Research Laboratory, University of California, Santa Barbara, California 93106, United States

[‡]Materials Department, University of California, Santa Barbara, California 93106, United States

[¶]Department of Chemistry and Argonne-Northwestern Solar Energy Research (ANSER) Center, Northwestern University, Evanston, Illinois 60208, United States

[§]Department of Chemistry and Biochemistry, University of California, Santa Barbara, California 93106, United States

[∥]Institute of Nanoscience and Nanotechnology, NCSR Demokritos, 15310 Athens, Greece

[⊥]Physics Department, National Technical University of Athens, 15780 Zografou, Athens, Greece

S Supporting Information

ABSTRACT: Stable s^2 lone pair electrons on heavy main-group elements in their lower oxidation states drive a range of important phenomena, such as the emergence of polar ground states in some ferroic materials. Here we study the perovskite halide CsSnBr$_3$ as an embodiment of the broader materials class. We show that lone pair stereochemical activity due to the Sn^{2+} s^2 lone pair causes a crystallographically hidden, locally distorted state to appear upon warming, a phenomenon previously referred to as emphanisis. The synchrotron X-ray pair distribution function acquired between 300 and 420 K reveals emerging asymmetry in the nearest-neighbor Sn–Br correlations, consistent with dynamic Sn^{2+} off-centering, despite there being no evidence of any deviation from the average cubic structure. Computation based on density functional theory supports the finding of a lattice instability associated with dynamic off-centering of Sn^{2+} in its coordination environment. Photoluminescence measurements reveal an unusual blue-shift with increasing temperature, closely linked to the structural evolution. At low temperatures, the structures reflect the influence of octahedral rotation. A continuous transition from an orthorhombic structure (Pnma, no. 62) to a tetragonal structure (P4/mbm, no. 127) is found around 250 K, with a final, first-order transformation at 286 K to the cubic structure (Pm$\bar{3}$m, no. 221).
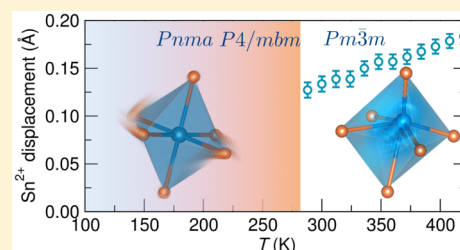
INTRODUCTION

Inorganic and hybrid main-group halide perovskites have attracted significant attention of late for their excellent performance in optoelectronic applications, ease of preparation, and abundant constituent elements.[1−7] In addition to being investigated for use in radiation detectors and light-emitting diodes,[8] the all-inorganic CsMX$_3$ (M = Ge, Sn, Pb; X = Cl, Br, I) perovskites offer an opportunity to understand the crystal chemistry of the divalent metal−halogen network without the added complexity introduced by the organic molecular ions present in the heavily studied organic−inorganic hybrids.[9−12]

These materials are distinguished from tetrahedral semi-conductors and from transition metal oxides in part by the presence of a s^2 lone pair on the divalent M-site cation. The lone pair gives rise to strong optical absorption near the bandgap and an unusual band structure, with the valence band comprising a mixture of cation s states and anion p states and three conduction bands comprised of cation p states.[11] A similar electronic structure gives rise to a lattice instability in divalent group IV chalcogenides[13] and monovalent group III halides.[14] Proximity to such a polar instability produces enhanced dielectric response and thus may contribute to effective screening of defects in semiconductors.[14,15] Recently, a locally distorted state was reported in rock-salt group IV chalcogenides (SnTe,[16] PbS, and PbTe[17]) upon warming on the basis of X-ray and neutron total scattering experiments, wherein the crystal retains long-range cubic symmetry but the cations move off their nominal sites in a spatially or temporally incoherent fashion. This phenomenon has been referred to as emphanisis, meaning the appearance of something (a low symmetry state) from nothing (a high symmetry state) upon warming, in a manner that is contrary to most crystals that attain lower symmetries upon cooling. On the basis of chemical and thermodynamic arguments, the authors proposed lattice expansion-induced lone pair stereochemical activity as the

mechanism for this unusual phenomenon, and in the case of SnTe found qualitative differences between this emergent high-temperature phase and the ferroic low-temperature phase. Following these reports, a number of articles have appeared, seeking to clarify the lattice dynamics and local structure of these materials based on ab initio calculations,[18−21] extended X-ray absorption fine structure (EXAFS) spectroscopy,[22,23] neutron scattering,[19,24,25] X-ray diffraction,[26] and piezoresponse force microscopy.[21] Most agree that a high degree of anharmonicity of the cation potential well exists within the region accessible at relevant thermal energies.

In contrast to systems that display such emphanisis, the typical phase evolution of polar insulators, including ferroelectric oxides, is from a centrosymmetric high-temperature phase to a noncentrosymmetric low-temperature phase (or sequence of phases) with spontaneous polarization. This conventional picture is true of materials with lone pair-bearing metals ($PbTiO_3$, $BiFeO_3$ with the lone pair on the A-site cations)[27,28] and those without ($BaTiO_3$, $KNbO_3$).[29,30] Local structure probes have revealed a more complex picture of the phase transitions in some of these materials, wherein disordered local cation displacements persist above the phase transition and average out crystallographically to a high-symmetry structure model.[31,32] Notably, these disordered phases are emergent from a low-temperature phase with ferroic displacements, rather than from a high-symmetry undistorted phase, as has been proposed in the group IV chalcogenides.

The instabilities associated with lone pair-bearing $d^{10}s^2$ cations and empty shell d^0 cations in high-symmetry environments are a consequence of the pseudo-Jahn−Teller effect,[33,34] and predictors of ferroelectric instability based on simple chemical and geometric factors have been enumerated.[13] On the basis of these factors, we selected $CsSnBr_3$ for study as an exemplar of the delicate balance of structural tendencies in the main-group halide perovskites. In $CH_3NH_3SnBr_3$, the larger A-site cation expands the lattice and leads to coherent Sn^{2+} displacements in the orthorhombic phase[35] and to local displacements in the cubic phase.[36] In contrast, $CH_3NH_3PbBr_3$ shows no signs of coherent displacements in the low-temperature phases[37] or local displacements in the cubic phase[36] due to the lowering of the Pb^{2+} lone pair levels associated with relativistic effects. This strong influence of the divalent cation is also evident in the iodides: the tendency for lone pair stereochemical activity is strong in $CsGeI_3$, resulting in a polar rhombohedral crystal structure with 3 + 3 Ge coordination at ambient temperatures,[9] while the high-performance photovoltaic $CH_3NH_3PbI_3$ adopts orthorhombic, tetragonal, and cubic phases without coherent Pb^{2+} displacements[38] and shows no signs of local displacements at ambient temperature.[39] $CsSnF_3$, with strong lone pair stereochemical activity due to the hard fluoride anions, exists not as a perovskite but rather as a salt of Cs^+ and $[SnF_3]^-$ pyramids.[40]

Here, we report the phase evolution of the halide perovksite $CsSnBr_3$ from 100 to 420 K, including the first observation of a dynamic instability in the cubic phase ($T > 290$ K) characterized by local off-centering of Sn^{2+} cations at elevated temperatures. In other words, $CsSnBr_3$ displays emphanisis, in a manner very similar to the chalcogenides such as PbTe. These local distortions are evident in the pair distribution function obtained from neutron and X-ray total scattering studies between 300 and 420 K. Ab initio calculations of lattice dynamics, electronic structure, and dielectric properties of $CsSnBr_3$ and related phases support this interpretation and

suggest that the s^2 lone pair electrons of the main-group cation are responsible for this instability. Photoluminescence measurements reveal a blue-shift of the bandgap with warming which becomes markedly more temperature-dependent in the cubic phase. We report the complete high resolution crystal structures for the cubic (300 K) and orthorhombic (100 K) phases of $CsSnBr_3$ from neutron and synchrotron X-ray powder diffraction and for the tetragonal (270 K) phase of $CsSnBr_3$ from synchrotron X-ray powder diffraction. The structures of the tetragonal and orthorhombic phases demonstrate that at reduced temperatures, the tendency for Sn^{2+} to off-center is suppressed by the competing tendency for octahedral rotations that enhance electrostatic binding and increase the coordination of the undersized A-site cation. Ab initio calculations of the lattice dynamics of the orthorhombic phase confirm that it is the ground state structure, highlighting the categorical difference between the phase evolution of ferroelectric oxides and that of $CsSnBr_3$, where cation displacements exist only at elevated temperatures.

■ EXPERIMENTAL SECTION

$CsSnBr_3$ was prepared by reacting $SnBr_2$ (Sigma-Aldrich, 20 mmol, 5.570 g) and CsBr (99.9% Sigma-Aldrich, 20 mmol, 4.256 g) in a fused SiO_2 tube (13 mm OD, 11 mm ID), which was evacuated to 10^{-3} mbar and flame-sealed. The silica tube was placed in a furnace and heated to 600 °C over 6 h, held at this temperature for 3 h, followed by cooling down to ambient temperature over 3 h. The reaction resulted in a shiny black ingot of $CsSnBr_3$. The ingot was isolated by breaking the ampule in a N_2-filled glovebox as a precautionary measure. The compound is air-stable and suffers only surface damage when exposed to humid air.

High-Q resolution X-ray diffraction data were collected from 100 to 300 K using the 11-BM beamline at the Advanced Photon Source (APS), Argonne National Laboratory (ANL), utilizing a calibrated wavelength of 0.45898 Å. The $CsSnBr_3$ sample (0.1 mmol, 27.8 mg) was transferred into a mortar and ground together with fused SiO_2 (0.9 mmol, 54 mg) into a homogeneous gray powder to reduce the absorption coefficient of the sample relative to the neat $CsSnBr_3$ material. The resulting powder was transferred to a fused SiO_2 capillary with a 0.5 mm OD and filled up to approximately 2 cm in height. Subsequently, powdered, fused SiO_2 was added and the capillary was evacuated to 10^{-3} mbar and flame-sealed through the fused SiO_2 powder to prevent the loosening of the powder during evacuation and to ensure a more homogeneous sealing of the capillary. Time-of-flight (TOF) neutron diffraction data were collected at 100 and 300 K on the POWGEN diffractometer at the Spallation Neutron Source (SNS), Oak Ridge National Laboratory (ORNL). The $CsSnBr_3$ ingot was broken into pieces, taking care to remove the top 1 to 2 mm that could be a potential source of impurities. Pieces of the ingot were transferred into a mortar and thoroughly ground to a fine powder. The powder was filled into a 6 mm vanadium can and was subsequently compressed tightly. The total mass of the sample for the neutron experiment was 4.381 g. The packed vanadium can was then sealed tightly under a N_2 atmosphere. Data were collected for a total time of 2 h on banks 2 and 4 with a central wavelength of the TOF neutrons chosen to be 1.066 and 2.665 Å, respectively. TOF neutron total scattering experiments were performed at 300 and 420 K utilizing the nanoscale ordered materials diffractometer (NOMAD) at the SNS located at ORNL with a collection time of approximately 2 to 4 h per sample.[41] The sample was the same as that for the POWGEN experiment. An empty 6 mm vanadium can was collected and subtracted as background. The pair distribution function (PDF), $G(r)$, was obtained by the transformation of the normalized total scattering function, $S(Q)$, with a $Q_{min} = 0.5$ Å^{-1} and $Q_{max} = 31.5$ Å^{-1}. Synchrotron X-ray total scattering measurements were collected on the 11-ID-B beamline at the APS located at ANL with a photon wavelength of 0.1430 Å from 100 to 420 K. A sample of fine powder,

obtained by means described above, was transferred into a Kapton capillary (1.1 mm OD, 1.0 mm ID) tightly compacted to ensure the maximum packing fraction. Both ends of the capillary were sealed with epoxy and stored in a N_2 atmosphere prior to the measurement. Data were collected every 2 min upon cooling at a rate of 6 K min^{-1}. Corrections to obtain the $S(Q)$ and subsequent Fourier transform with a Q_{max} of 23 Å^{-1} to obtain the $G(r)$ was performed using the program PDFgetX2.[42]

Rietveld refinements were carried out on the diffraction data to obtain the average crystallographic structure using the GSAS software suite with the EXPGUI interface.[43,44] The local structure was investigated via analysis of the real-space PDF using the PDFgui software suite.[45] Correlated motion in the PDF was modeled using the sratio and rcut parameters, which account for effects on the PDF due to correlated motion of rigid structural units. An rcut value of 5 Å was specified, which corresponds to the approximate Br–Br distance in the SnBr$_6$. Crystal structures were visualized using the VESTA suite of programs.[46]

All calculations were performed with the Vienna Ab initio Simulation Package (VASP),[47−50] which implements the Kohn−Sham formulation of density functional theory (DFT) using a plane-wave basis set and the projector augmented wave formalism.[51,52] The generalized gradient approximation (GGA) was employed using the Perdew−Burke−Ernzerhof (PBE) exchange and correlation functional for total energy and electronic structure calculations,[53] and the PBEsol functional for calculations of phonon dispersions and dielectric properties.[54] In each case, calculations were performed from structures with lattice parameters relaxed with the corresponding functional. Valence electron configurations were as follows: Cs, $5s^25p^66s^1$; Br, $4s^24p^5$; Sn, $5s^24d^{10}5p^2$; Pb, $6s^25d^{10}6p^2$; and Ca, $3s^23p^64s^2$. Plane wave basis set cutoff energies and Γ-centered Brillouin zone sampling densities were chosen based on the convergence of total energy in structure relaxations (PBE: 500 eV cutoff, 8×8×8 Monkhorst−Pack sampling,[55] a = 5.894 Å; PBEsol: 520 eV cutoff, 11×11×11 Monkhorst−Pack sampling, a = 5.759 Å). For calculation of the electronic density of states, a denser 24×24×24 k-point mesh was employed. Born effective charge tensors, high-frequency dielectric tensors, and static dielectric tensors (including local field effects) were calculated using density functional perturbation theory (DFPT).[56]

Energy surfaces for displacement of the divalent cation were calculated for both a primitive cell and a 2×2×2 supercell, wherein total energy per formula unit was evaluated as a function of rigid cation displacement along the high-symmetry directions and of lattice parameter contraction or expansion. For the 2×2×2 supercell study, all symmetrically distinct combinations of high symmetry real-space displacement directions ($\langle 100 \rangle$, $\langle 110 \rangle$, and $\langle 111 \rangle$) and high-symmetry reciprocal-space vectors (Γ, X, M, and R) modulating the displacements from site-to-site were considered. The k-point density was kept the same for the supercell calculations.

The frozen phonon approach was employed to calculate the force constants for CsSnBr$_3$. Forces resulting from single atomic displacements (0.1 Å) were collected with VASP, and a least-squares fit between perturbations and collected forces was used to determine harmonic force constants.[57] The Born effective charges and dielectric tensors evaluated from DFPT were used to calculate the nonanalytic correction for the dynamical matrix due to long-range Coulomb interactions. For the cubic phase, a 3×3×3 supercell (135 atoms) was used with a 4×4×4 Γ-centered k-point mesh, while for the orthorhombic phase, a 2×1×2 supercell (80 atoms) with a 4×6×4 Γ-centered k-point mesh was employed.

To screen candidate crystal structures for the low-temperature phase of CsSnBr$_3$, symmetrized displacement modes associated with M_3^+ and R_4^+ irreducible representations of the M and R points of the first Brillouin zone in the parent $Pm\bar{3}m$ structure were found with the ISODISTORT[58] module of ISOTROPY (ISOTROPY Software Suite, iso.byu.edu). The 15 unique octahedral tilt systems as described by Howard and Stokes[59] were then enumerated through the application of the M_3^+ and R_4^+ displacement modes of the Br sublattice. Structural relaxations of all tilt systems were carried out in 2×2×2 supercells of the primitive cell with a 6×6×6 k-point mesh centered at the Γ point

until the forces on atoms reached <10 meV Å^{-1}. Symmetries of the relaxed structures were verified using the FINDSYM[60] module of ISOTROPY.

Differential scanning calorimetry was recorded on ground 5.9 mg sample using a DSC Q-2000 calorimeter from TA Instruments. The temperature was swept from 123 to 323 K at a rate of 10 K min^{-1} for 2 cycles. Visible−near-infrared photoluminescence spectra were recorded in a THMS600PS Linkam optical cell with a heating-freezing stage, under dynamic vacuum. The excitation beam (532 nm laser, 10 mW) was focused on the sample via a lens with a focal length of 75 mm in a quasi-backscattering geometry. Emitted light was analyzed in a double monochromator and detected with a photomultiplier.

■ RESULTS AND DISCUSSION

Average and Local Structure of Cubic CsSnBr$_3$. Joint Rietveld refinements of the X-ray and neutron diffraction data at 300 K (Figure 1 and Table 2) indicate the data is well-
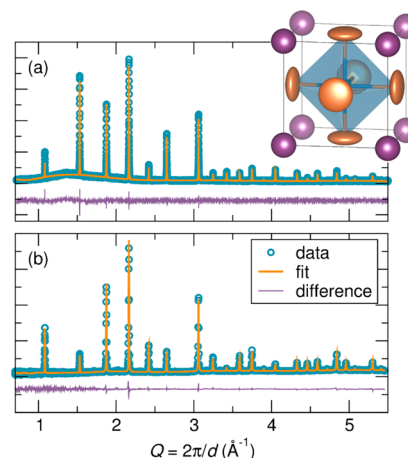

Figure 1. Fits obtained from the joint Rietveld refinement against $Pm\bar{3}m$ of (a) X-ray and (b) TOF neutron diffraction data collected at 300 K. Inset: analysis of the diffraction data indicates enlarged ADPs (shown at 90% probability) on the Cs and Br sites. In particular, Br ADPs are anisotropically enlarged perpendicular to the Sn−Br bond, highlighting the presence of dynamic octahedral rotations in the flexible Sn−Br framework.

described by the cubic space group $Pm\bar{3}m$ (no. 221) with Cs$^+$ in the 1a Wyckoff site at (0, 0, 0), Sn^{2+} in the 1b site at $(\frac{1}{2}, \frac{1}{2}, \frac{1}{2})$, and Br$^-$ in the 3c site at $(0, \frac{1}{2}, \frac{1}{2})$. The cation sites are modeled with isotropic atomic displacement parameters (ADPs, reported in U_{iso}), while the Br anions exhibit large anisotropic ADPs perpendicular to the Sn−Br bond of the SnBr$_6$ octahedral units, indicating a high degree of structural disorder of the Br atoms normal to the Sn−Br−Sn bonds. These large transverse displacements arise from the flexible nature of the partially covalent Sn−Br octahedral network, as well as the very low Cs−Br bond valence, and suggest there are dynamic octahedral rotations at this temperature.

A qualitative comparison of the X-ray PDFs between 300 and 420 K (Figure 2) reveals the emergence of a peak asymmetry of the first peak to high-r upon warming, which corresponds to the Sn−Br correlation in CsSnBr$_3$. However, no apparent changes in this temperature range can be distinguished over 2 to 20 Å as the data tends toward an average, crystallographic picture. Peak asymmetry of the first Sn−Br correlation can also be observed in the neutron PDF and is illustrated in Figure S1.

Fits of the X-ray PDFs between 300 and 420 K were performed against the $Pm\bar{3}m$ model obtained from the joint
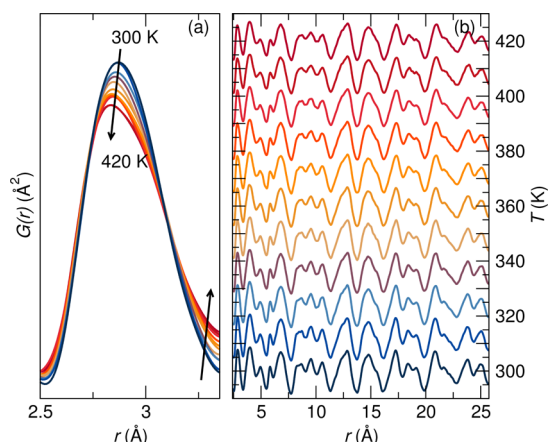
Figure 2. X-ray PDF data for $CsSnBr_3$ over a range from 300 to 420 K. (a) Emergence of peak asymmetry in the Sn−Br correlation distance can be observed upon warming, while (b) the data over 2 to 20 Å indicate no apparent change over longer r correlations.
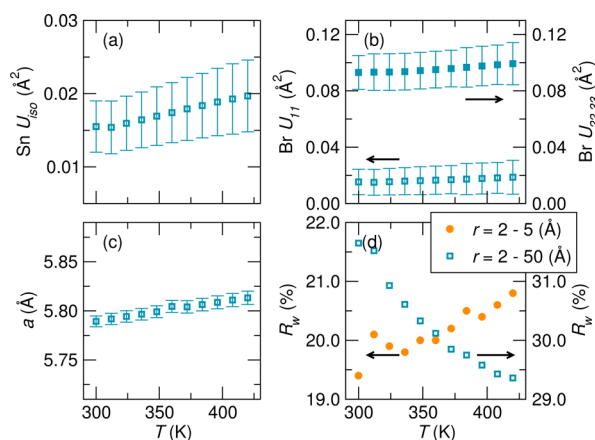

Figure 3. Select parameters obtained from fitting of the X-ray PDFs from 300 to 420 K over a fit range from 2 to 5 Å (orange ●) and 2 to 50 Å (blue □) with structural model $Pm\bar{3}m$. (a) Sn isotropic and (b) Br anisotropic ADPs both increase with increasing temperature. (c) Comparison of the trend in lattice parameters with increasing temperature indicates an increase for the 50 Å fit due to thermal expansion. (d) R_w values obtained from the temperature series indicates a decreasing R_w with temperature over the 50 Å fit (i.e., the cubic model becomes a better description of the long-range symmetry with warming), whereas an increasing R_w is observed for the 5 Å fit (i.e., the cubic model becomes a worse description of the local structure with warming).

Rietveld refinement of the diffraction data at 300 K over ranges from 2 to 5 Å and 2 to 50 Å. Results are summarized in Figure 3. The ADP values obtained from the 2 to 5 Å fit were highly correlated and did not yield a stable refinement, and therefore, only ADPs from the 2 to 50 Å fit are shown. In general, ADPs increase with temperature as expected due to increased thermal motion of atoms about their crystallographic sites. The Br ADPs remain anisotropic as was observed in the Rietveld refinement. Due to the large transverse motion of the Br atoms with respect to the Sn−Br bond, the evolution of the lattice parameters over the 2 to 50 Å fit range was investigated. Similar large transverse motion of anions has been observed in ReO_3, which may be responsible for apparent negative thermal expansion in the material.[61,62] However, lattice parameters exhibit an increase with temperature, following typical thermal

expansion behavior. By looking at the R_w goodness-of-fit parameter, it can be seen that the R_w values against the cubic model show a decrease with increasing temperature over the 2 to 50 Å fit range. This indicates that the data are better described by a cubic space group as the temperature increases. This is in agreement with the average, crystallographic structure at these temperatures. However, the R_w values of the data over a 2 to 5 Å fit range increase with temperature, indicating the data is more poorly described by the cubic model as the temperature increases: the sample is locally deviating from cubic symmetry upon warming.

For the cubic structure, we would expect a single, symmetric Sn−Br correlation in the PDF, in contrast to the observed peak asymmetry over the 2 to 5 Å range. Geometrical considerations of the local atomic interactions could help elucidate the origin of the observed asymmetry in the Sn−Br correlation. For example, the enlarged perpendicular anisotropic ADPs of the Br atoms could result in a distribution of Sn−Br correlations at and above the nominal Sn−Br bond distance, which would appear as peak tailing to high r. Alternatively, a rhombohedral off-centering of the Sn^{2+} (toward the face of the $SnBr_6$ octahedra along the [111] crystallographic direction) would result in two Sn−Br correlation distances. If this off-centering is dynamic, this could appear as an asymmetric peak at the nominal Sn−Br correlation distance.

To investigate the effect of anisotropic Br ADPs on the PDF, three $Pm\bar{3}m$ structural models were constructed and fit over a 2 to 5 Å range against the X-ray PDF at 420 K: isotropic Br ADPs set to the U_{eq} value obtained from the 300 K Rietveld refinement ($U_{11} = U_{22} = U_{33} = 0.107$), anisotropic Br ADPs set to the values obtained from the 300 K Rietveld refinement ($U_{11} = 0.026$; $U_{22} = U_{33} = 0.1443$), and anisotropic Br ADPs with an exaggerated perpendicular component ($U_{11} = 0.026$; $U_{22} = U_{33} = 0.4$) (see Figure 4). For all three models, the Br ADPs were held constant while other parameters (overall scale, lattice
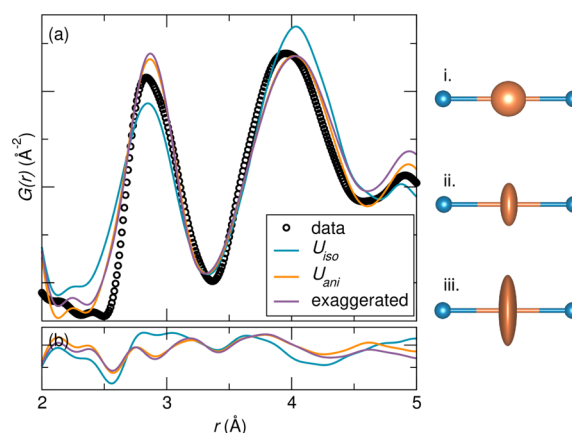

Figure 4. (a) Fits of the X-ray PDF at 420 K with three models of the Br ADPs in space group $Pm\bar{3}m$: isotropic ADPs (U_{iso}; $U_{11} = U_{22} = U_{33}$), anisotropic ADPs obtained from the joint Rietveld refinements of the average structure (U_{ani}; $U_{11} < U_{22} = U_{33}$), and exaggerated anisotropic ADPs (exaggerated; $U_{11} \ll U_{22} = U_{33}$). (b) Comparison of the difference curves for the fits of the three models indicates none are able to capture the peak asymmetry of the Sn−Br correlation at approximately 2.8 Å, but anisotropic ADPs are necessary to accurately model the second peak, comprised of Cs−Br and Br−Br correlations. Illustrations of the Sn−Br−Sn interactions in the three models are shown to the right: i, U_{iso}; ii, U_{ani}; and iii, exaggerated, with ADPs shown at 90% probability.

parameter, correlated motion, Sn U_{iso}, and Cs U_{iso}) were allowed to refine freely. It is observed that the anisotropic ADPs are essential for an accurate description of the second peak in the PDF, as this peak is dominated by Br-dependent correlations (Cs−Br and Br−Br). While the anisotropic ADPs do seem to do a better job of describing the first PDF peak by an effective shift in the central r-distance of the modeled Sn−Br correlation, they are unable to describe the observed asymmetry. This is indicative that the data cannot be explained by anisotropic ADPs alone; however, it must be recognized that this may be due to a limitation of PDFgui, which applies the harmonic approximation and thus generates Gaussian peak shapes.[63,64] Therefore, if an harmonic approximation is assumed, a two-peak model, such as that of a rhombohedrally distorted local symmetry, may provide a better description of this peak within the limitations of the analysis.

To model local Sn^{2+} displacement directions against the X-ray PDF data at 420 K, various crystallographic structures with prototypical ferroic displacements in perovskite materials were used: cubic $Pm\bar{3}m$ (no Sn^{2+} displacement), tetragonal $P4mm$ (no. 99) (Sn^{2+} displacement along the $\langle 100 \rangle$ toward a corner of the $SnBr_6$ octahedron), orthorhombic $Amm2$ (no. 38) (Sn^{2+} displacement along the $\langle 110 \rangle$ toward an edge of the $SnBr_6$ octahedron), and rhombohedral $R3m$ (no. 160) (Sn^{2+} displacement along the $\langle 111 \rangle$ toward a face of the $SnBr_6$ octahedron). Fits to the various models are shown in Figure 5. Starting
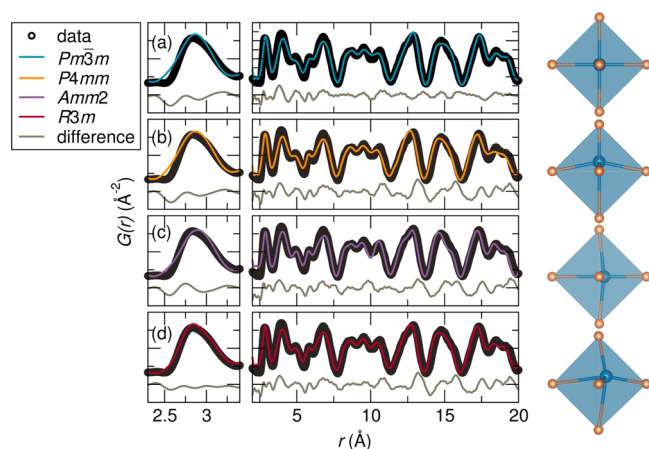

Figure 5. Fits of the X-ray PDF at 420 K against known prototypical ferroelectric perovskite space groups: (a) $Pm\bar{3}m$ (cubic, no Sn displacement), (b) $P4mm$ (tetragonal, Sn displacement along $\langle 100 \rangle$), (c) $Amm2$ (orthorhombic, Sn displacement along $\langle 110 \rangle$), and (d) $R3m$ (rhombohedral, Sn displacement along $\langle 111 \rangle$). A rhombohedral displacement of approximately 0.2 Å provides the best description of the asymmetric Sn−Br peak over a fit range from 2 to 5 Å, while cubic symmetry more accurately captures the features over a longer r-range (2 to 20 Å). Illustrations of the Sn^{2+} displacements in the $SnBr_6$ octahedra are shown to the right of each fit.

structural models were obtained by transforming the refined cubic $Pm\bar{3}m$ structure into the various lower symmetry space groups, which were subsequently refined against the 300 K Rietveld data. To avoid excessive correlations of parameters during the refinements of the PDF data, anisotropic Br ADPs were fixed to those obtained from the Rietveld fits, while other parameters were allowed to refine.

As previously seen in the 300 to 420 K temperature series, the cubic space group does not describe the asymmetric shape of the first peak in the X-ray PDF at 420 K. A similar fit is

obtained with the tetragonal $P4mm$ structure. Displacement of Sn^{2+} toward the corner of an $SnBr_6$ octahedron results in a narrow distribution of one short, four intermediate, and one long bond lengths, which effectively creates peak tailing to both high- and low-r of the main Sn−Br correlation. Similarly, a displacement of Sn^{2+} toward the edge of the octahedron results in a distribution of two short, two intermediate, and two long bond lengths, and once again does not describe the asymmetric shape. However, displacement toward the face of the octahedron results in three short and three long Sn−Br bond distances, which would appear as two peaks in the PDF. Indeed, over a 2 to 5 Å fit range, the rhombohedral model provides the best comparative fit to the data, capturing the peak asymmetry as a superposition of two Sn−Br correlations with a small r separation, corresponding to an Sn^{2+} off-centering of approximately 0.2 Å. This observed off-centering could arise from stereochemical activity of the $5s^2$ pair of electrons associated with Sn^{2+} driven by lattice expansion upon warming. The local rhombohedral distortion appears as two overlapping peaks, in contrast to that of the local rhombohedral distortion observed in $BaTiO_3$,[31,65] where there are two distinct first correlation peaks. This is proposed to be an effect of dynamic displacement within the octahedra rather than the static displacement observed in $BaTiO_3$. This modeling approach limits the resulting local structure models to those of cation displacements along high symmetry directions. More complex stochastic approaches, such as those recently employed in understanding the nature of distortions in $BaTiO_3$,[66] suggest the way forward for bias-free determination of local distortions and their correlations but are beyond the scope of this work. Nonetheless, our results do indicate that local Sn^{2+} displacements are the likely cause of the observed peak asymmetry at elevated temperatures, and that among the high symmetry directions, these displacements are preferentially along $\langle 111 \rangle$. This is also corroborated by DFT calculations as described in the next subsection.

The degree of Sn^{2+} displacement from the center of the $SnBr_6$ octahedron as a function of temperature was determined by refinement of the X-ray PDF data against the rhombohedral
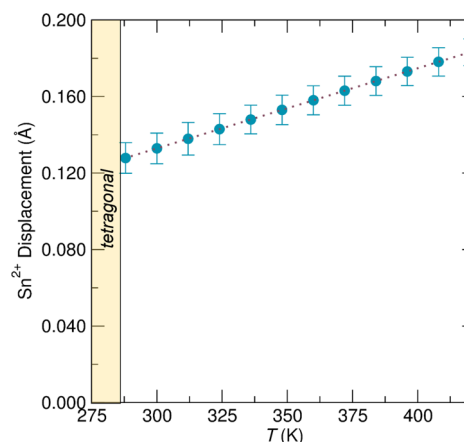

Figure 6. Evolution of Sn^{2+} displacement from the center of the $SnBr_6$ octahedron with increasing temperature as determined from fitting the X-ray PDF over a range from 2 to 5 Å against the rhombohedral $R3m$ model. Displacement from the center increases with increasing temperature. On cooling, the displacement does not reach zero (Sn^{2+} in the center of the octahedron) in the cubic phase due to the onset of a phase transition to a tetragonal structure at 286 K.

$R3m$ model (see Figure 6). Refinements were performed over a fit range from 2 to 5 Å and a temperature range from 300 to 420 K. The degree of displacement is seen to increase with temperature and is attributed to enhanced stereochemical activity with expansion of the lattice. This is reported to drive a crossover from a local, lone pair-inactive state to a local, lone pair-active state in rock-salt tin and lead chalcogenides.[16] In contrast with the chalcogenides, the local displacement of Sn^{2+} in cubic $CsSnBr_3$ does not appear to go continuously to zero displacement on cooling and is instead suppressed discontinuously as the crystal undergoes a phase transition to a tetragonal structure at 286 K (vide infra).

Ab Initio Studies of Cubic $CsSnBr_3$. Ab initio calculations of lattice dynamics, electronic structure, and dielectric properties of $CsSnBr_3$ are consistent with this propensity for off-centering of Sn^{2+} and confirm that these displacements are preferentially along ⟨111⟩. Additionally, comparison with isostructural but chemically distinct phases illustrates the importance of s^2 lone pair electrons in this coupled electronic–lattice instability. The electronic band structure and orbital-projected density of states, calculated at the PBE level with and without spin–orbit coupling (SOC), are presented in Figure 7. The PBE exchange and correlation
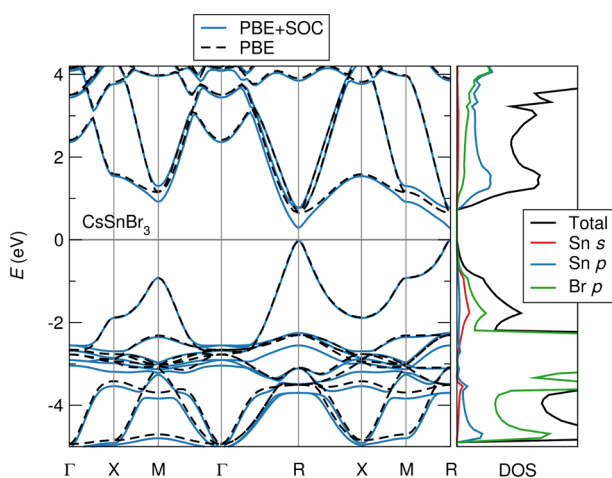

Figure 7. Electronic band structure and projected density of states (DOS) of $CsSnBr_3$, illustrating the "inverted" band structure typical of main-group halide perovskites. The valence band is formed from the antibonding interaction between Sn(s) and Br(p) orbitals. The regions near the conduction band minimum are triply degenerate in the absence of spin orbit coupling and are primarily derived from Sn(p) orbitals. The modest effect of spin orbit coupling is evident.

functional is known to poorly reproduce excited state properties and thus underestimate bandgaps. Apart from the magnitude of the bandgap, our results agree in the essential aspects with those of Huang and Lambrecht, from self-consistent quasiparticle calculations.[11] Similar to other inorganic main-group halide perovskites, the band structure is "inverted," with a single valence band with primarily Sn(s)–Br(p) antibonding character and a triply degenerate (in the absence of SOC) conduction band minimum of primarily Sn(p) character.[11,67]

The Sn^{2+} lone pair electrons are rather shallow relative to the Fermi energy. Strong overlap between occupied Sn(s) and Br(p) states produces a σ-like band at ∼4 eV below E_f and the σ^*-like valence band. This interaction pushes the antibonding Sn(s) states up in energy, bringing them close in energy to the

unoccupied Sn(p) states, which tends to promote lone pair stereochemical activity.[68−72] Additionally, cross-gap mixing of cation (p) and anion (p) states is evident, which has been associated with elevated Born effective charges, giant splitting between longitudinal and transverse optical modes (LO/TO splitting), and polar instability in perovskite oxides.[73−76] Systems with these electronic features exhibit a strong electron–phonon coupling (and atomic displacement–polarization coupling), with implications for charge transport and defect tolerance.[14]

Comparison with isostructural $CsPbBr_3$ and $CsCaBr_3$ allows us to examine the influence of the s^2 lone pair electrons on the electronic structure and lattice dynamics: Pb^{2+} is predicted to have a lesser tendency for stereochemical activity due to greater relativistic stabilization of the lone pair,[13] and Ca^{2+} lacks a lone pair as it is fully oxidized to the electron configuration of Ar. The electronic band structures and densities of states of $CsPbBr_3$ and $CsCaBr_3$ are presented in Figures S2 and S3. The band structure of $CsPbBr_3$ is similar to that of $CsSnBr_3$, but the competing effects of longer metal–Br bond length, reduced ionicity of metal–Br interaction, and stronger spin–orbit coupling result in a wider bandgap and larger carrier effective masses at this level of theory. The large electronegativity difference between Ca and Br causes $CsCaBr_3$ to be an insulator, with rather localized electronic states. We return to the comparison with these related phases presently.

Calculated Born effective charges and dielectric responses are also indicative of a polar instability, and are presented in Table 1. The Born charges of $CsSnBr_3$ and $CsPbBr_3$ are significantly

Table 1. Born Effective Charges (Z_M^*) of the Central Metal Cation M^{2+}, High-Frequency Dielectric Permittivity (ϵ_∞), and Static Dielectric Permittivity (ϵ_0) for $CsMBr_3$

	Z_M^* (e)	ϵ_∞	ϵ_0
$CsSnBr_3$	5.1	6.5	68.3
$CsPbBr_3$	4.3	4.8	22.1
$CsCaBr_3$	2.5	3.1	17.5

elevated above the nominal divalent charge, consistent with substantial covalency and a large polarization response to ion displacement (or equivalently, a large force on the ions in response to electric fields). $CsCaBr_3$, in which the divalent cation lacks a lone pair of s^2 electrons, stands apart: the Ca^{2+} Born charge is much more similar to the formal charge for this highly electropositive cation, which implies the restoring forces are reasonably described by a simple ionic picture.

The same relative trend is present in both the high frequency and static permittivities. There is a very large difference between the purely electronic and combined electronic–ionic dielectric response in $CsSnBr_3$, which is equivalent by the Lydanne-Sachs-Teller relation to a large LO/TO splitting. In the divalent group IV chalcogenides, Waghmare and co-workers have identified large LO/TO splitting as a strong predictor for lone pair stereochemical activity.[13] Du and Singh have identified a similar giant LO/TO splitting in the radiation detector TlBr (with similar electronegativity difference to Sn and Br) and have proposed this proximal instability as a mechanism for defect screening and robust carrier transport.[14] While the static dielectric constants of $CsPbBr_3$ and $CsCaBr_3$ are both substantial (due in part to the soft potential well for Cs^+ displacement, which is highly undercoordinated in the cubic phase, vide infra), they are much lower than that of
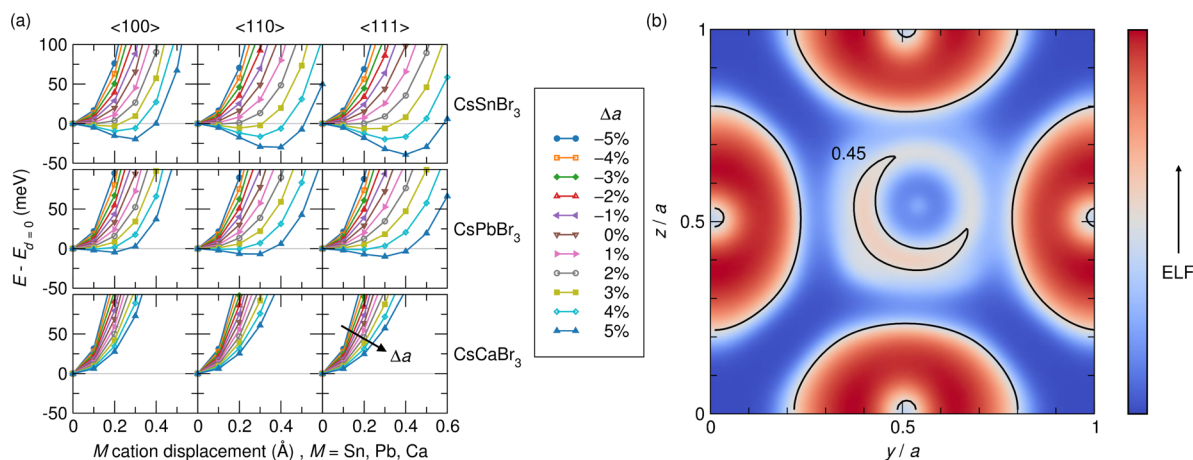
Figure 8. (a) Energy landscape for cation displacement in cubic CsMBr$_3$ along high-symmetry directions at various compressed and expanded lattice parameters, $a = a_{nom}(1 + \Delta a)$. An instability is evident in CsSnBr$_3$ and CsPbBr$_3$: an energy minimum develops off the nominal crystallographic position upon lattice expansion. This effect is notably absent in CsCaBr$_3$, which lacks a lone pair of s^2 electrons. (b) The electron localization function (ELF) of CsSnBr$_3$ on a (200) slice of the unit cell (a plane through the nominal Sn site), with Sn^{2+} displaced 0.4 Å, along [111] and $\Delta a =$ 5%, corresponding to the deepest well in (a). The contour at ELF = 0.45 shows clearly the localization of the 5s^2 lone pair into a lobe opposite the direction of ion displacement. The regions of strong localization around Br$^-$ are indicative of the nonbonding electrons in the Br p orbitals orthogonal to the sp hybridized Sn−Br bonds.

CsSnBr$_3$. This is consistent with our prediction that CsPbBr$_3$ should be further from this off-centering instability[13] and that there is no off-centering instability at all for CsCaBr$_3$ (all three systems exhibit an instability to octahedral rotations in the cubic phase due to the nonunity tolerance factors, but this is not reflected in the dielectric response because these modes do not contribute to the polarizability of the crystal).

Energy surfaces for displacement of the octahedrally coordinated divalent cation along the high-symmetry directions for CsSnBr$_3$, CsPbBr$_3$, and CsCaBr$_3$ are given in Figure 8a as a function of lattice expansion or contraction. All directions are referenced to the parent cubic cell. Such calculations on a single formula unit necessarily imply a ferroic ordering of cation displacements. Nonetheless, important qualitative differences emerge, and we find that these features are robust in more complex supercell calculations (vide infra). As there is minimal band reorganization due to spin−orbit coupling (Figure 7), we omit this computationally costly correction for our lattice dynamical studies.

At the relaxed value of the lattice parameter ($\Delta a = 0\%$), we see simple potential wells for cation displacement, with $\langle 111 \rangle$ the softest directions. Upon lattice expansion, the potential wells in CsSnBr$_3$ and CsPbBr$_3$ soften substantially, taking on a highly anharmonic shape. Above a critical value of the lattice expansion (~2% for CsSnBr$_3$, ~4% for CsPbBr$_3$), the energy minimum moves off of the nominal crystallographic site. Notably, for lattice parameters of a few percent over the relaxed value (consistent with the extremely large linear coefficient of thermal expansion, $\alpha_a = 35$ ppm K^{-1}, determined from real-space fitting to the CsSnBr$_3$ X-ray PDF), we observe energy minima at displacements on the order of tenths of an Angstrom, with depths on the order of $k_B T$. These displacements are well within the resolution of PDFs calculated from X-ray and neutron scattering and are in essential agreement with the separation of the high-r shoulder and the main peak for the first Sn−Br correlation from experiment at elevated temperatures (Figures 2 and 5). The shallow depth of the energy wells relative to the available thermal energy is consistent with these displacements being dynamic in nature. At the relaxed lattice

parameter, cubic CsSnBr$_3$ and CsPbBr$_3$ are both proximate to an instability characterized by dynamic off-centering of the lone pair-bearing main-group cation. This instability can be activated by lattice expansion. CsPbBr$_3$ is further from this instability as expected from the lesser tendency for lone pair stereochemical activity of Pb^{2+}.[13]

Importantly, this feature is absent in the perovskite CsCaBr$_3$, which lacks a lone pair on the divalent cation. Ca^{2+} is chosen for comparison because of its identical ionic radius to Sn^{2+} in octahedral coordination, as calculated from bond valence sums in oxides.[77,78] Because effective ionic size depends on the ligands, CsSnBr$_3$ and CsCaBr$_3$ have different relaxed lattice parameters. To ensure that a similar feature does not develop on further lattice expansion, calculations on CsCaBr$_3$ were carried out up to a lattice parameter of 10% over the relaxed value. No such feature developed, and the data is omitted from Figure 8a for clarity. There is no covalent driving force for Ca^{2+} displacements in cubic CsCaBr$_3$ because there are no lone pair electrons to mix with the orbitals of the ligands.

Visualization of electronic structure in real space via the electron localization function (ELF) provides additional information about the role of the lone pair in this lattice instability. The ELF is a real space scalar field which measures the spatially resolved effect of Pauli repulsion (essentially, the difference in kinetic energy between otherwise equivalent systems of Fermions and bosons), and which may be used to classify electrons as bonding, nonbonding, or core based on topological analysis.[79] A two-dimensional (2D) slice of the ELF of CsSnBr$_3$ along (200) is presented in Figure 8b, for the case where Sn^{2+} is displaced along [111]. An asymmetric lobe of elevated localization opposite to the direction of cation displacement is indicative of the broken inversion symmetry of the lone pair that has become stereochemically active. In the undistorted case, the lone pair retains octahedral symmetry and the corresponding local maximum of the ELF occurs on a symmetric shell about Sn^{2+} rather than at a point away from the nucleus as it does here. The stereochemically active lone pair localizes as a lobe opposite the direction of cation displacement.
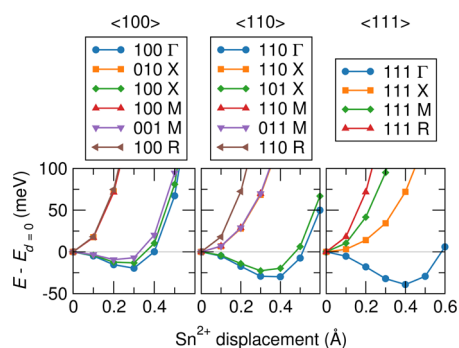
Figure 9. Energy landscape for symmetrically distinct high symmetry displacement patterns of Sn^{2+} for a 2×2×2 supercell, with expanded lattice parameter, Δa = 5%. The nominal real-space directions of cation displacement are indicated, as well as the high-symmetry reciprocal-space vectors describing the alternation of displacements from octahedron to octahedron along each of the cubic axes. Only Sn^{2+} is displaced; the A and X sublattices are unperturbed.

To investigate the importance of spatial coherence (ferroic ordering) of cation displacements, we consider high symmetry displacement patterns of Sn^{2+} in a 2×2×2 supercell. The resulting energy surfaces are given in Figure 9 for an expanded lattice parameter (Δa = 5%). The anion and A-site sublattices are rigidly fixed, and all distinct combinations of high-symmetry real-space cation displacement directions and high-symmetry reciprocal-space vectors describing the spatial modulation of displacements are considered.

The Γ-like displacements are identical to the ferroic case presented above and are the most energetically favorable for all directions considered. For displacements along $\langle 100 \rangle$ and $\langle 110 \rangle$, other orderings where the sign of the displacements are modulated along vectors orthogonal to the displacements themselves are similarly favorable (100 X, 001 M, 101 X; no such scenarios are possible for $\langle 111 \rangle$ displacements). Thus, the dominant unfavorable interaction is the displacement of neighboring Sn^{2+} ions toward each other, suggesting that displacements are locally coherent (in fact, this feature may indicate a tendency for "chainlike" ordering of displacements, as in $BaTiO_3$[80]). The potential well is sufficiently shallow relative to the available thermal energy that the cations do not localize and break global inversion symmetry but rather explore this 8-well potential dynamically (local minima along each of the $\langle 111 \rangle$ directions). Big box calculations that consider more complex displacement patterns (that is, reciprocal-space vectors other than only those at the Brillouin zone edges) may provide more information about the nature of fluctuating polar nanodomains, though we expect that such energy surfaces would be bracketed by the stiffest and softest curves presented in Figure 9.

Impact of Dynamic Off-Centering on Properties. In addition to its importance for our fundamental understanding of lone pair electrons in the solid state and the coupling between electronic structure and lattice dynamics, this dynamic lone pair stereochemical activity has significant implications for material properties and functionality. Indeed, any property which couples to the lattice will be influenced by the strong anharmonicity that emerges on warming.

The experimentally observed cell volume, extracted from real-space fitting of the X-ray PDFs over the 20 Å, to 50 Å, range, and the temperature dependence of the photoluminescence (PL) emission peak energy is presented in

Figure 10 (raw PL spectra are given in Figure S4). Of note, volumetric thermal expansion is extremely rapid (β = 121 ppm
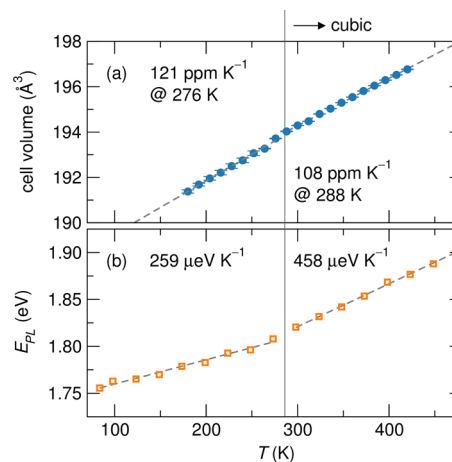

Figure 10. Experimental evolution of unit cell volume and photoluminescence (PL) emission peak energy, E_{PL}, with temperature. (a) The volumetric thermal expansion coefficient is 12% larger below the tetragonal−cubic transition than in the cubic phase and is among the highest reported for any inorganic solid.[10] (b) The energy of the PL peak blue-shifts with temperature between 80 and 480 K, consistent with the effects of volumetric expansion on the "orbital-inverted" electronic structure. The blue-shift becomes 77% more rapid in the cubic phase, despite the more gradual thermal expansion, suggesting a substantial contribution from dynamic Sn^{2+} displacements.

K^{-1} at 276 K, fully two-thirds the value for liquid Hg, and just smaller than that of $CsSnI_3$[10]). This rapid thermal expansion may itself be a consequence of lone pair induced anharmonicity. Upon warming to the cubic phase, β is somewhat reduced, possibly due to a negative contribution from dynamic octahedral tilts as in ReO_3[61] and ScF_3.[81]

To understand the rapid blue-shift of the PL emission peak, we computed the electronic bandgap and band edge positions as functions of lattice expansion and Sn^{2+} displacement. The results, as well as a qualitative band diagram constructed from molecular orbitals, are presented in Figure 11. The bandgap of $CsSnBr_3$ widens on lattice expansion due to simultaneous narrowing and stabilization of both the valence and conduction bands, consequences of their antibonding character. This is in opposition to the computed behavior of $CsCaBr_3$, which, like group IV, III−V, and II−VI semiconductors, has a bandgap between bonding and antibonding states. Ferroic Sn^{2+} displacements along [111] are also seen to widen the gap by reducing orbital overlap from a maximum in the high symmetry state.

Experimentally, the PL peak (a proxy for the bandgap, barring abrupt changes in defect or excitonic levels) is observed to blue-shift with warming for all temperatures studied, as expected based on volumetric expansion and the underlying electronic structure. However, the blue-shift becomes 77% more rapid in the cubic phase, despite the reduced volumetric thermal expansion coefficient. Though inclusion of electron−phonon coupling is required for a comprehensive treatment of finite temperature effects, the magnitude of this trend suggests a substantial contribution from the local, dynamic Sn^{2+} displacements that are present in the cubic phase.

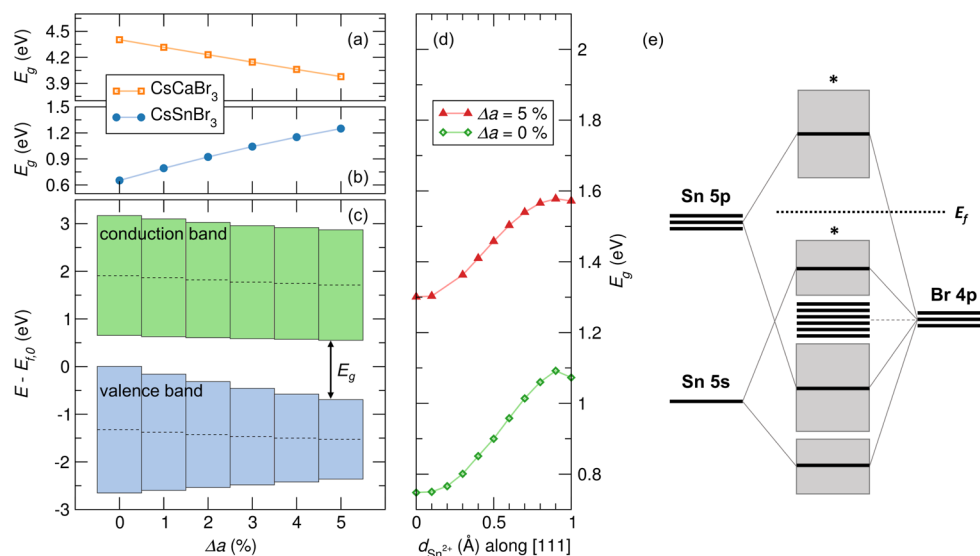The anharmonic potential surface for cation displacement associated with emphanisis also gives rise to an elevated

Figure 11. Evolution of the computed (PBE) bandgap, E_g, with lattice parameter expansion, Δa, for cubic (a) $CsCaBr_3$ and (b) $CsSnBr_3$. (c) Evolution of the $CsSnBr_3$ valence band and conduction band edges with lattice expansion, showing the simultaneous narrowing and stabilization of both bands due to weakened antibonding interactions. Band centers are indicated by dashed lines, and all are plotted on a common energy scale by aligning the energy of dispersionless Cs states. This is contrary to the bandgap evolution of tetrahedral semiconductors[82] and of isostructural $CsCaBr_3$, which lacks an s^2 lone pair. (d) Evolution of the computed (PBE) bandgap with rhombohedral Sn^{2+} displacement in $CsSnBr_3$. Cation displacement serves to widen the bandgap, as has been calculated for frozen soft phonons in PbTe.[18] (e) Qualitative band diagram for three-dimensional (3D) corner-sharing $[SnBr_3]^{-1}$ octahedral network which reflects the calculated electronic structure in Figure 7.

dielectric response, as we have calculated for the relaxed cubic cell in the previous section (the response should be substantially greater at finite temperatures, given the massive positive thermal expansion). In principle, the ionic part of the dielectric response can be tuned to be arbitrarily large by bringing the system to the brink of the ferroelectric transition. This can be achieved by alloying of a lighter halogen, a lighter carbon-group element, or a larger A-site cation such as methylammonium or formamidinium which will increase the propensity for lone pair stereochemical activity.[13] Because of the importance of defect screening for carrier transport, such tuning can be used to enhance carrier mobilities, as has been shown in pseudo-Jahn–Teller perovskite oxides.[15] In the high-performance perovskite halide $CH_3NH_3PbI_3$, the large polarizability associated with the lone pair and with molecular reorientation may explain why carrier scattering is dominated by phonons rather than charged impurities.[83−85]

The details of charge transport in the halide perovskites remain mysterious, in particular the peculiar existence of extremely long carrier diffusion lengths[4,86,87] and lifetimes[87,88] despite modest mobilities.[89,90] Experimental and theoretical reports propose various mechanisms for reconciling these observations and the temperature dependence of carrier mobilities, including the formation of large polarons which increase carrier effective mass and protect against bimolecular recombination,[89] free carrier transport limited by acoustic[83,85] or optical[91] phonons, and photon recycling.[7] The dynamic lone pair stereochemical activity we observe in $CsSnBr_3$ has implications for carrier recombination and transport in the halide perovskites beyond enhanced dielectric screening of charged defects. The short-range spatial coherence of Sn^{2+} fluctuations suggested by our ab initio calculations implies the creation of polar nanodomains that will tend to separate electrons and holes in real space, thus reducing bimolecular recombination.[5,92,93] Additionally, Sn^{2+} displacements along certain directions split the otherwise degenerate conduction

band minima in momentum due to the local symmetry-breaking. Such momentum-splitting, arising either from local distortions[94,95] or spin−orbit coupling[96,97] has been proposed to limit carrier recombination.[94,96,97] Further, the off-centering tendency of the divalent cation contributes to the lattice deformability, which would aid the formation of large polarons which may protect carriers from bimolecular recombination.[89]

Emergent anharmonicity in the phonon spectrum associated with lone pair stereochemical activity also has implications for phonon lifetimes and associated properties. The large fluctuating Pb^{2+} displacements in PbTe at elevated temperatures have been correlated with strong scattering of acoustic phonons and corresponding low lattice thermal conductivity, a fortuitous attribute for a high-performance thermoelectric material.[98−100] One expects that the extremely low thermal conductivity of $CH_3NH_3PbI_3$ is in part due to this lone pair-driven anharmonicity.[101]

Competing Instabilities at Lower Temperatures: Structural Transitions. From laboratory X-ray diffraction, $CsSnBr_3$ is reported to undergo three successive phase transitions from the cubic perovskite structure upon cooling: to tetragonal $P4/mbm$ (no. 127) at 292 K, to $P4_12$ (no. 90) at 274 K, and to an undetermined monoclinic phase at 247 K.[102] The cubic to tetragonal phase transition has also been observed in ^{119}Sn Mössbauer,[103] ultraviolet photoelectron, and X-ray photoelectron spectroscopy.[104] Mössbauer additionally suggests a transition at approximately 260 K. While the cubic-to-tetragonal phase transition at 292 K is widely reported,[102−105] the successive phase evolution upon cooling remain ambiguous.

High-resolution Bragg scattering and differential scanning calorimetry (Figure S5) reveal a first-order phase transition at 286 K and a continuous phase transition around 250 K. Candidate space groups for the low-temperature (100 K) phase were screened with DFT as discussed in the Experimental Section: the 15 unique octahedral tilt systems[59] were seeded with displacements of the Br sublattice and allowed to relax in a

$2\times2\times2$ supercell. Resulting energies, referenced to the cubic aristotype ($a^0a^0a^0$ in Glazer notation[106]), are presented in
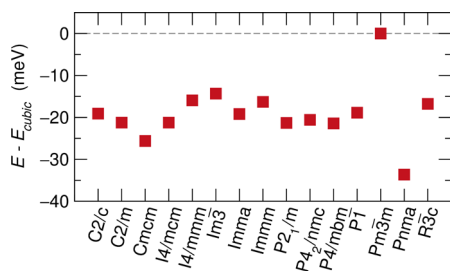

Figure 12. Total energy (per formula unit) of relaxed structures with the 15 unique octahedral tilt systems relative to the energy of the cubic $Pm\overline{3}m$ aristotype. The structure with $Pnma$ space group symmetry is substantially lower in energy than any other, suggesting a ground state structure with $a^-b^+a^-$ tilts. This model is confirmed by our Rietveld analysis of X-ray and neutron diffraction experiments (Figure 13).

Figure 12. It is seen that the structure with the $Pnma$ space group is lower in energy than any other tilt system, suggesting a ground state structure with $a^-b^+a^-$ tilts. On the basis of this screening, a joint Rietveld refinement was performed on the X-ray and neutron diffraction data at 100 K against the orthorhombic $Pnma$ (no. 62) structure with Cs^+ in the $4c$ Wyckoff site at $(x, \frac{1}{4}, z)$, Sn^{2+} in the $4b$ site at $(0, 0, \frac{1}{2})$, and Br^- in the $4c$ and $8d$ sites at $(x, \frac{1}{4}, z)$ and (x, y, z), respectively. The resulting fit and select crystallographic data are summarized in Figure 13a,b and Table 2. Both sets of data
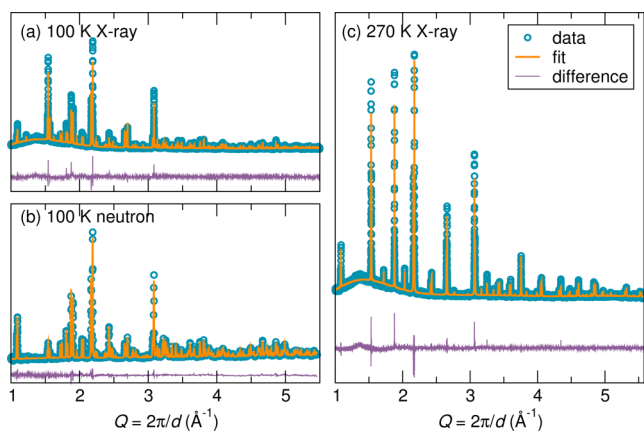

Figure 13. Fits obtained from the Rietveld refinements of the low-temperature phases of $CsSnBr_3$. The joint refinement of the (a) X-ray and (b) TOF neutron diffraction data at 100 K indicates the data is well fit against orthorhombic $Pnma$. (c) Refinement of the X-ray diffraction data at 270 K shows the data is well fit with tetragonal $P4/mbm$.

are indexed and fit well by this structural model. ADPs are reduced in comparison to those of the higher-temperature structures, and this indicates that the disorder is a dynamic, temperature-driven effect. Ab initio calculations of the phonon dispersion for this $Pnma$ phase (Figure S7) reveal no unstable modes, suggesting that there is no further phase evolution on cooling below 100 K. Calculations of the bond valence sums (BVS)[107,108] for Cs^+ in a 12-coordinate site using bond valence parameters extrapolated by Brese and O'Keeffe,[109] give BVS of 0.86 and 0.53 at 100 and 300 K, respectively. Cs is severely

under-bonded in the cubic phase, but combined Cs and Br displacements in the orthorhombic phase raise the BVS closer to the nominal value of 1, optimizing Cs coordination and stabilizing the $Pnma$ structure. Fits of the 100 K X-ray PDF data over a 2 to 5 Å range against the refined average $Pnma$ structure show the local structure of $CsSnBr_3$ is described well by this model (Figure S8).

Rietveld refinement of the X-ray diffraction data collected at 270 K was performed against a structural model with space group $P4/mbm$ with Cs^+ in the $2c$ Wyckoff site at $(\frac{1}{2}, 0, \frac{1}{2})$, Sn^{2+} in the $2a$ site at $(0, 0, 0)$, and Br^- in the $2d$ and $4g$ sites at $(0, 0, \frac{1}{2})$ and $(x, y, 0)$, respectively. The resulting fit and select crystallographic data are summarized in Figure 13c and Table 2.

Table 2. Select Crystallographic Data from the Rietveld Refinements of Powder Synchrotron X-ray and Neutron Diffraction Data of $CsSnBr_3$ at 100, 270, and 300 K

temperature (K)	100	270	300
data sets	X-ray, neutron	X-ray	X-ray, neutron
space group	$Pnma$	$P4/mbm$	$Pm\overline{3}m$
a (Å)	8.1965(2)	8.1789(2)	5.8043(3)
b (Å)	11.5830(3)	8.17989(2)	5.8043(3)
c (Å)	8.0243(2)	5.8193(2)	5.8043(3)
volume (Å³)	761.82(3)	389.29(3)	195.546(5)
Sn U_{iso} (Å²)	0.013(5)	0.024(2)	0.022(5)
Cs U_{11} (Å²)	0.033(5)	0.082(5)	0.077(2)
Cs U_{22} (Å²)	0.021(4)	0.082(5)	0.077(2)
Cs U_{33} (Å²)	0.038(5)	0.057(8)	0.077(2)
Cs U_{12} (Å²)	0.0	−0.032(9)	0.0
Cs U_{13} (Å²)	−0.008(4)	0.0	0.0
Cs U_{23} (Å²)	0.0	0.0	0.0
Br1 U_{11} (Å²)	0.033(4)	0.090(9)	0.02(2)
Br1 U_{22} (Å²)	0.010(3)	0.090(9)	0.148(3)
Br1 U_{33} (Å²)	0.042(4)	0.018(9)	0.148(3)
Br1 U_{12} (Å²)	0.0	0.0	0.0
Br1 U_{13} (Å²)	−0.007(4)	0.0	0.0
Br1 U_{23} (Å²)	0.0	0.0	0.0
Br2 U_{11} (Å²)	0.020(2)	0.052(7)	—
Br2 U_{22} (Å²)	0.032(2)	0.052(7)	—
Br2 U_{33} (Å²)	0.023(2)	0.119(9)	—
Br2 U_{12} (Å²)	0.0	0.041(8)	—
Br2 U_{13} (Å²)	−0.008(2)	0.0	—
Br2 U_{23} (Å²)	0.002(2)	0.0	—
Sn−Br1 (Å)	2.9245(7)	2.9096(9)	2.9021(5)
Sn−Br2 (Å)	2.927(3)	2.910(9)	—
Sn−Br1−Sn (deg)	164.0(2)	180	180
Sn−Br2−Sn (deg)	156.8(4)	167.0(5)	—
R_w (%)	5.48	9.21	4.31

Refinement against the $P4/mbm$ structure provided a reasonable fit of the data (R_w = 9.21%). Refinement against the reported $P42_12$ structure[102] was performed but yielded a poorer fit (R_w = 9.58%) and is shown in Figure S9. Additionally, assignment of $P4/mbm$ space group symmetry is consistent with calculations of the preferred octahedral tilts for perovskite bromides[110] and with calorimetry (Figure S5): the transition from $Pnma$ to $P4/mbm$ is allowed to be continuous under Landau theory, while $Pnma$ to $P42_12$ is not (ISOTROPY Software Suite, iso.byu.edu). As expected, the BVS for Cs (0.63 at 270 K) is intermediate to those in the cubic and orthorhombic phases.
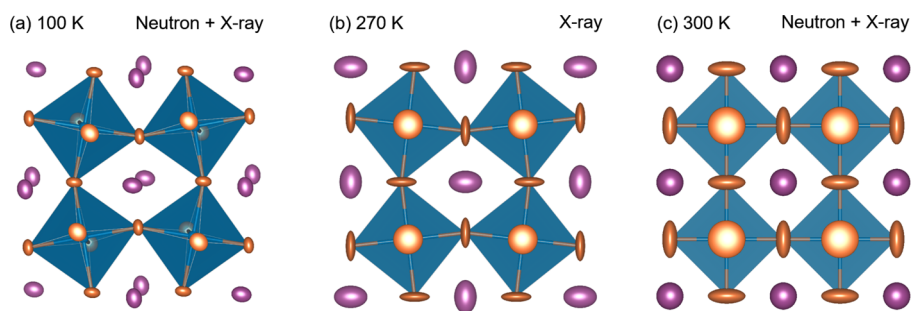
Figure 14. Evolution of the crystallographic structures of $CsSnBr_3$ upon warming from (a) orthorhombic *Pnma* at 100 K, to (b) tetragonal *P4/mbm* at 270 K, to (c) cubic *Pm$\bar{3}$m* at 300 K. ADPs for all structures shown at 90% probability.

Through the application of Rietveld analysis of X-ray and neutron diffraction data, it was determined that $CsSnBr_3$ adopts the following structures: orthorhombic *Pnma* below 250 K, tetragonal *P4/mbm* between 250 and 286 K, and cubic *Pm$\bar{3}$m* above 286 K. The successive phases are visualized in Figure 14. Upon cooling, the structure undergoes an in-phase rotation of the $SnBr_6$ octahedra about the *c* axis corresponding to an $a^0a^0c^+$ tilt, which is consistent with calculations of the preferred octahedral tilts for perovskite bromides.[110] Additional out-of-phase rotation is observed at 100 K, corresponding to an $a^-b^+a^-$ tilt. In addition to the onset of rotational transitions, the isotropic ADP of Sn^{2+} is reduced upon cooling, implying the disorder around the crystallographic site is dynamic in nature and off-centering is suppressed at low temperatures. There is an observed increase in the Sn—Br bond lengths and decrease in the Sn—Br—Sn bond angles with cooling, indicating the degree of overlap between the Sn(p) and Sn(s)—Br(p) orbitals decreases as the structure undergoes the successive rotational phase transitions. The reduction of orbital overlap results in less propensity for stereochemical activity of the Sn^{2+} lone pair and thus less tendency for Sn^{2+} off-centering. Additionally, octahedral rotations bring the ions closer together, resulting in a larger electrostatic penalty for Sn^{2+} displacement. These observations illustrate the competing tendencies for lone pair stereochemical activity and octahedral rotations. At elevated temperatures, the former dominates, while the latter emerges upon cooling and suppresses off-centering of Sn^{2+}. A discussion of the competition between covalency and ionicity for the related perovskite $CsPbF_3$ is given by Smith and co-workers,[111] which displays both $a^-a^-a^-$ octahedral rotations and Pb^{2+} displacements in the low-temperature phase.[112]

CONCLUSION

The main-group halide perovskite $CsSnBr_3$ exhibits competing tendencies for local Sn^{2+} off-centering and $SnBr_6$ octahedral rotations. Due to the presence of the $5s^2$ lone pair, an instability emerges in the cubic phase as the lattice is expanded on warming. This instability is characterized by dynamic off-centering of Sn^{2+} in its coordination environment and the localization of the stereochemically active $5s^2$ lone pair as a lobe opposite the direction of cation displacement, providing evidence of emphanisis in this material. These displacements occur preferentially along ⟨111⟩ and likely exhibit some short-range coherence. While this locally distorted state is "crystallographically hidden" (the only clue being elevated thermal displacement parameters for Sn^{2+} when refined in a high-symmetry environment), it is evident in the pair distribution function as emergent asymmetry in the first Sn—Br correlation and is corroborated by ab initio calculations of the lattice

dynamics, dielectric properties, and electronic structure of the crystal. Similar calculations on isostructural $CsPbBr_3$ and $CsCaBr_3$ indicate that this off-centering instability is present but weaker in $CsPbBr_3$, in accordance with existing theory of lone pair stereochemical activity, and is entirely absent in $CsCaBr_3$, which lacks a lone pair on the divalent cation. These local cation displacements drive a rapid blue-shift of the bandgap on warming which is observed in photoluminescence measurements. Upon cooling, $CsSnBr_3$ undergoes successive phase transitions driven by octahedral rotations, with the unit cell transforming from cubic to tetragonal to orthorhombic. In crystal structure models for the tetragonal and orthorhombic phases, reduced thermal displacement parameters for Sn^{2+} suggest that there are no coherent or local cation displacements that are not captured by the model: lone pair stereochemical activity is suppressed by the octahedral rotations. The phenomenon is likely to be quite general, and one would expect to observe emphanisis also in the cubic phases of $CsSnCl_3$ and $CsSnI_3$ with the strength of the effect increasing as the halogen atoms become lighter and more electronegative.[13]

The unusual structure evolution of $CsSnBr_3$ sheds further light on the role of lone pair electrons in extended inorganic solids. Chemical tuning to bring about this proximal instability in the halide perovskites offers a means to tailor the properties of these curious and promising semiconductors: by exploiting lone pair stereochemistry, it is possible to engineer lattice polarizability that enhances dielectric response and promotes polaron formation, thermal conductivity reduction, anomalous bandgap evolution with temperature, and possibly other functionalities.

■ ASSOCIATED CONTENT

ⓢ Supporting Information

The Supporting Information is available free of charge on the ACS Publications website at DOI: 10.1021/jacs.6b06287.

$CsSnBr_3$ neutron PDF at 300 and 420 K, calculated electronic structure of $CsPbBr_3$ and $CsCaBr_3$, temperature-dependent $CsSnBr_3$ photoluminescence, differential scanning calorimetry of $CsSnBr_3$, calculated phonon dispersions for the cubic and orthorhombic phases of $CsSnBr_3$, $CsSnBr_3$ X-ray PDF at 100 K, Rietveld fit of $CsSnBr_3$ X-ray diffraction data at 270 K in space group $P42_12$ (PDF)

■ AUTHOR INFORMATION

Corresponding Author

*seshadri@mrl.ucsb.edu

Article

Author Contributions

#D.H.F. and G.L. contributed equally to the manuscript.

Notes

The authors declare no competing financial interest.

■ REFERENCES

(1) Kojima, A.; Teshima, K.; Shirai, Y.; Miyasaka, T. J. Am. Chem. Soc. 2009, 131, 6050−6051.
(2) Kim, H.-S.; Lee, C.-R.; Im, J.-H.; Lee, K.-B.; Moehl, T.; Marchioro, A.; Moon, S.-J.; Humphry-Baker, R.; Yum, J.-H.; Moser, J. E.; Grätzel, M.; Park, N.-G. Sci. Rep. 2012, 2, 591.
(3) Xing, G.; Mathews, N.; Sun, S.; Lim, S. S.; Lam, Y. M.; Gratzel, M.; Mhaisalkar, S.; Sum, T. C. Science 2013, 342, 344−347.
(4) Stranks, S. D.; Eperon, G. E.; Grancini, G.; Menelaou, C.; Alcocer, M. J. P.; Leijtens, T.; Herz, L. M.; Petrozza, A.; Snaith, H. J. Science 2013, 342, 341−344.
(5) Frost, J. M.; Butler, K. T.; Brivio, F.; Hendon, C. H.; Van Schilfgaarde, M.; Walsh, A. Nano Lett. 2014, 14, 2584−2590.
(6) Ponseca, C. S.; Savenije, T. J.; Abdellah, M.; Zheng, K.; Yartsev, A.; Pascher, T.; Harlang, T.; Chabera, P.; Pullerits, T.; Stepanov, A.; Wolf, J.-P.; Sundström, V. J. Am. Chem. Soc. 2014, 136, 5189−5192.
(7) Pazos-Outon, L. M.; Szumilo, M.; Lamboll, R.; Richter, J. M.; Crespo-Quesada, M.; Abdi-Jalebi, M.; Beeson, H. J.; Vrucinic, M.; Alsari, M.; Snaith, H. J.; Ehrler, B.; Friend, R. H.; Deschler, F. Science 2016, 351, 1430−1433.
(8) Stoumpos, C. C.; Malliakas, C. D.; Peters, J. A.; Liu, Z.; Sebastian, M.; Im, J.; Chasapis, T. C.; Wibowo, A. C.; Chung, D. Y.; Freeman, A. J.; Wessels, B. W.; Kanatzidis, M. G. Cryst. Growth Des. 2013, 13, 2722−2727.
(9) Stoumpos, C. C.; Frazer, L.; Clark, D. J.; Kim, Y. S.; Rhim, S. H.; Freeman, A. J.; Ketterson, J. B.; Jang, J. I.; Kanatzidis, M. G. J. Am. Chem. Soc. 2015, 137, 6804−6819.
(10) Chung, I.; Song, J.-H.; Im, J.; Androulakis, J.; Malliakas, C. D.; Li, H.; Freeman, A. J.; Kenney, J. T.; Kanatzidis, M. G. J. Am. Chem. Soc. 2012, 134, 8579−8587.
(11) Huang, L.-y.; Lambrecht, W. R. L. Phys. Rev. B: Condens. Matter Mater. Phys. 2013, 88, 165203.
(12) Patrick, C. E.; Jacobsen, K. W.; Thygesen, K. S. Phys. Rev. B: Condens. Matter Mater. Phys. 2015, 92, 201205.
(13) Waghmare, U. V.; Spaldin, N. A.; Kandpal, H. C.; Seshadri, R. Phys. Rev. B: Condens. Matter Mater. Phys. 2003, 67, 125111.
(14) Du, M.-H.; Singh, D. J. Phys. Rev. B: Condens. Matter Mater. Phys. 2010, 81, 144114.
(15) Siemons, W.; McGuire, M. A.; Cooper, V. R.; Biegalski, M. D.; Ivanov, I. N.; Jellison, G. E.; Boatner, L. A.; Sales, B. C.; Christen, H. M. Adv. Mater. 2012, 24, 3965−3969.
(16) Knox, K. R.; Bozin, E. S.; Malliakas, C. D.; Kanatzidis, M. G.; Billinge, S. J. L. Phys. Rev. B: Condens. Matter Mater. Phys. 2014, 89, 014102.
(17) Bozin, E. S.; Malliakas, C. D.; Souvatzis, P.; Proffen, T.; Spaldin, N. A.; Kanatzidis, M. G.; Billinge, S. J. L. Science 2010, 330, 1660−1663.
(18) Zhang, Y.; Ke, X.; Kent, P. R. C.; Yang, J.; Chen, C. Phys. Rev. Lett. 2011, 107, 175503.
(19) Li, C. W.; Ma, J.; Cao, H. B.; May, A. F.; Abernathy, D. L.; Ehlers, G.; Hoffmann, C.; Wang, X.; Hong, T.; Huq, A.; Gourdon, O.; Delaire, O. Phys. Rev. B: Condens. Matter Mater. Phys. 2014, 90, 214303.
(20) Chen, Y.; Ai, X.; Marianetti, C. A. Phys. Rev. Lett. 2014, 113, 105501.
(21) Aggarwal, L.; Banik, A.; Anand, S.; Waghmare, U. V.; Biswas, K.; Sheet, G. Journal of Materiomics 2016, 2, 196−202.
(22) Keiber, T.; Bridges, F.; Sales, B. C. Phys. Rev. Lett. 2013, 111, 095504.
(23) Mitrofanov, K. V.; Kolobov, A. V.; Fons, P.; Krbal, M.; Shintani, T.; Tominaga, J.; Uruga, T. Phys. Rev. B: Condens. Matter Mater. Phys. 2014, 90, 1−6.
(24) Jensen, K. M. Ø.; Božin, E. S.; Malliakas, C. D.; Stone, M. B.; Lumsden, M. D.; Kanatzidis, M. G.; Shapiro, S. M.; Billinge, S. J. L. Phys. Rev. B: Condens. Matter Mater. Phys. 2012, 86, 085313.
(25) Knight, K. S. J. Phys.: Condens. Matter 2014, 26, 385403.
(26) Kastbjerg, S.; Bindzus, N.; Søndergaard, M.; Johnsen, S.; Lock, N.; Christensen, M.; Takata, M.; Spackman, M. A.; Brummerstedt Iversen, B. Adv. Funct. Mater. 2013, 23, 5477−5483.
(27) Sawaguchi, E. J. Phys. Soc. Jpn. 1953, 8, 615−629.
(28) Baettig, P.; Seshadri, R.; Spaldin, N. A. J. Am. Chem. Soc. 2007, 129, 9854−9855.
(29) Hewat, A. W. Ferroelectrics 1973, 6, 215−218.
(30) Hewat, A. W. J. Phys. C: Solid State Phys. 1973, 6, 2559−2572.
(31) Kwei, G. H.; Billinge, S. J. L.; Cheong, S.-W.; Saxton, J. G. Ferroelectrics 1995, 164, 57−73.
(32) Ravel, B.; Stern, E. A.; Vedrinskii, R. I.; Kraizman, V. Ferroelectrics 1998, 206, 407−430.
(33) Bersuker, I. Phys. Lett. 1966, 20, 589−590.
(34) Bersuker, I. B. Chem. Rev. 2013, 113, 1351−1390.
(35) Swainson, I.; Chi, L.; Her, J.-H.; Cranswick, L.; Stephens, P.; Winkler, B.; Wilson, D. J.; Milman, V. Acta Crystallogr., Sect. B: Struct. Sci. 2010, 66, 422−429.
(36) Worhatch, R. J.; Kim, H.; Swainson, I. P.; Yonkeu, A. L.; Billinge, S. J. L. Chem. Mater. 2008, 20, 1272−1277.
(37) Swainson, I.; Hammond, R.; Soullière, C.; Knop, O.; Massa, W. J. Solid State Chem. 2003, 176, 97−104.
(38) Weller, M. T.; Weber, O. J.; Henry, P. F.; Di Pumpo, A. M.; Hansen, T. C. Chem. Commun. 2015, 51, 4180−4183.
(39) Choi, J. J.; Yang, X.; Norman, Z. M.; Billinge, S. J. L.; Owen, J. S. Nano Lett. 2014, 14, 127−133.
(40) Tran, T. T.; Halasyamani, P. S. J. Solid State Chem. 2014, 210, 213−218.
(41) Neuefeind, J.; Feygenson, M.; Carruth, J.; Hoffmann, R.; Chipley, K. K. Nucl. Instrum. Methods Phys. Res., Sect. B 2012, 287, 68−75.
(42) Qiu, X.; Thompson, J. W.; Billinge, S. J. L. J. Appl. Crystallogr. 2004, 37, 678−678.
(43) Larson, A. C.; Dreele, R. B. V. LAUR; Technical Report no. 86-748; Los Alamos National Laboratory: Los Alamos, NM, 2000.
(44) Toby, B. H. J. Appl. Crystallogr. 2001, 34, 210−213.

(45) Farrow, C. L.; Juhás, P.; Liu, J. W.; Bryndin, D.; Božin, E. S.; Bloch, J.; Proffen, T.; Billinge, S. J. L. *J. Phys.: Condens. Matter* **2007**, *19*, 335219.

(46) Momma, K.; Izumi, F. *J. Appl. Crystallogr.* **2011**, *44*, 1272−1276.

(47) Kresse, G.; Hafner, J. *Phys. Rev. B: Condens. Matter Mater. Phys.* **1993**, *47*, 558−561.

(48) Kresse, G.; Hafner, J. *Phys. Rev. B: Condens. Matter Mater. Phys.* **1994**, *49*, 14251−14269.

(49) Kresse, G.; Furthmüller, J. *Phys. Rev. B: Condens. Matter Mater. Phys.* **1996**, *54*, 11169−11186.

(50) Kresse, G.; Furthmüller, J. *Comput. Mater. Sci.* **1996**, *6*, 15−50.

(51) Blöchl, P. E. *Phys. Rev. B: Condens. Matter Mater. Phys.* **1994**, *50*, 17953−17979.

(52) Kresse, G.; Joubert, D. *Phys. Rev. B: Condens. Matter Mater. Phys.* **1999**, *59*, 1758−1775.

(53) Perdew, J. P.; Burke, K.; Ernzerhof, M. *Phys. Rev. Lett.* **1996**, *77*, 3865−3868.

(54) Perdew, J. P.; Ruzsinszky, A.; Csonka, G. I.; Vydrov, O. A.; Scuseria, G. E.; Constantin, L. A.; Zhou, X.; Burke, K. *Phys. Rev. Lett.* **2008**, *100*, 136406.

(55) Monkhorst, H. J.; Pack, J. D. *Phys. Rev. B* **1976**, *13*, 5188−5192.

(56) Gajdoš, M.; Hummer, K.; Kresse, G.; Furthmüller, J.; Bechstedt, F. *Phys. Rev. B: Condens. Matter Mater. Phys.* **2006**, *73*, 1−9.

(57) Chen, M.-H.; Emly, A.; Van der Ven, A. *Phys. Rev. B: Condens. Matter Mater. Phys.* **2015**, *91*, 214306.

(58) Campbell, B. J.; Stokes, H. T.; Tanner, D. E.; Hatch, D. M. *J. Appl. Crystallogr.* **2006**, *39*, 607−614.

(59) Howard, C. J.; Stokes, H. T. *Acta Crystallogr., Sect. B: Struct. Sci.* **1998**, *54*, 782−789.

(60) Stokes, H. T.; Hatch, D. M. *J. Appl. Crystallogr.* **2005**, *38*, 237−238.

(61) Chatterji, T.; Henry, P. F.; Mittal, R.; Chaplot, S. L. *Phys. Rev. B: Condens. Matter Mater. Phys.* **2008**, *78*, 3−8.

(62) Rodriguez, E. E.; Llobet, A.; Proffen, T.; Melot, B. C.; Seshadri, R.; Littlewood, P. B.; Cheetham, A. K. *J. Appl. Phys.* **2009**, *105*, 11490110.1063/1.3120783.

(63) Egami, T.; Billinge, S. J. L. *Underneath the Bragg Peaks: Structural Analysis of Complex Materials*; Elsevier Ltd.: Oxford, UK, 2003.

(64) Božin, E. S.; Juhás, P.; Billinge, S. J. L. In *Characterization of Semiconductor Heterostructures and Nanostructures*, 2nd ed.; Lamberti, C., Agostini, G., Eds.; Elsevier B.V., 2013; pp 229−257.

(65) Page, K.; Proffen, T.; Niederberger, M.; Seshadri, R. *Chem. Mater.* **2010**, *22*, 4386−4391.

(66) Senn, M. S.; Keen, D. A.; Lucas, T. C. A.; Hriljac, J. A.; Goodwin, A. L. *Phys. Rev. Lett.* **2016**, *116*, 207602.

(67) Brgoch, J.; Lehner, A. J.; Chabinyc, M. L.; Seshadri, R. *J. Phys. Chem. C* **2014**, *118*, 27721−27727.

(68) Watson, G. W.; Parker, S. C.; Kresse, G. *Phys. Rev. B: Condens. Matter Mater. Phys.* **1999**, *59*, 8481.

(69) Seshadri, R.; Baldinozzi, G.; Felser, C.; Tremel, W. *J. Mater. Chem.* **1999**, *9*, 2463−2466.

(70) Seshadri, R.; Hill, N. A. *Chem. Mater.* **2001**, *13*, 2892−2899.

(71) Seshadri, R. *Proc. - Indian Acad. Sci., Chem. Sci.* **2001**, *113*, 487−496.

(72) Walsh, A.; Payne, D. J.; Egdell, R. G.; Watson, G. W. *Chem. Soc. Rev.* **2011**, *40*, 4455−4463.

(73) Cohen, R. E. *Nature* **1992**, *358*, 136−138.

(74) Zhong, W.; King-Smith, R. D.; Vanderbilt, D. *Phys. Rev. Lett.* **1994**, *72*, 3618−3621.

(75) Posternak, M.; Resta, R.; Baldereschi, A. *Phys. Rev. B: Condens. Matter Mater. Phys.* **1994**, *50*, 8911−8914.

(76) Ghosez, P.; Michenaud, J.-P.; Gonze, X. *Phys. Rev. B: Condens. Matter Mater. Phys.* **1998**, *58*, 6224−6240.

(77) Shannon, R. D.; Prewitt, C. T. *Acta Crystallogr., Sect. B: Struct. Crystallogr. Cryst. Chem.* **1969**, *25*, 925−946.

(78) Shannon, R. D. *Acta Crystallogr., Sect. A: Cryst. Phys., Diffr., Theor. Gen. Crystallogr.* **1976**, *32*, 751−767.

(79) Silvi, B.; Savin, A. *Nature* **1994**, *371*, 683−686.

(80) Ghosez, P.; Cockayne, E.; Waghmare, U. V.; Rabe, K. M. *Phys. Rev. B: Condens. Matter Mater. Phys.* **1999**, *60*, 836−843.

(81) Greve, B. K.; Martin, K. L.; Lee, P. L.; Chupas, P. J.; Chapman, K. W.; Wilkinson, A. P. *J. Am. Chem. Soc.* **2010**, *132*, 15496−15498.

(82) O'Donnell, K. P.; Chen, X. *Appl. Phys. Lett.* **1991**, *58*, 2924−2926.

(83) Oga, H.; Saeki, A.; Ogomi, Y.; Hayase, S.; Seki, S. *J. Am. Chem. Soc.* **2014**, *136*, 13818−13825.

(84) Savenije, T. J.; Ponseca, C. S.; Kunneman, L.; Abdellah, M.; Zheng, K.; Tian, Y.; Zhu, Q.; Canton, S. E.; Scheblykin, I. G.; Pullerits, T.; Yartsev, A.; Sundström, V. *J. Phys. Chem. Lett.* **2014**, *5*, 2189−2194.

(85) Milot, R. L.; Eperon, G. E.; Snaith, H. J.; Johnston, M. B.; Herz, L. M. *Adv. Funct. Mater.* **2015**, *25*, 6218−6227.

(86) Dong, Q.; Fang, Y.; Shao, Y.; Mulligan, P.; Qiu, J.; Cao, L.; Huang, J. *Science* **2015**, *347*, 967−970.

(87) Shi, D.; et al. *Science* **2015**, *347*, 519−522.

(88) Zhang, M.; Yu, H.; Lyu, M.; Wang, Q.; Yun, J.-H.; Wang, L. *Chem. Commun.* **2014**, *50*, 11727−11730.

(89) Zhu, X.-Y.; Podzorov, V. *J. Phys. Chem. Lett.* **2015**, *6*, 4758−4761.

(90) Brenner, T. M.; Egger, D. A.; Rappe, A. M.; Kronik, L.; Hodes, G.; Cahen, D. *J. Phys. Chem. Lett.* **2015**, *6*, 4754−4757.

(91) Filippetti, A.; Mattoni, A.; Caddeo, C.; Saba, M. I.; Delugas, P. *Phys. Chem. Chem. Phys.* **2016**, *18*, 15352−15362.

(92) Quarti, C.; Mosconi, E.; De Angelis, F. *Chem. Mater.* **2014**, *26*, 6557−6569.

(93) Ma, J.; Wang, L.-w. *Nano Lett.* **2015**, *15*, 248−253.

(94) Motta, C.; El-Mellouhi, F.; Kais, S.; Tabet, N.; Alharbi, F.; Sanvito, S. *Nat. Commun.* **2015**, *6*, 7026.

(95) Beecher, A. N.; Semonin, O. E.; Skelton, J. M.; Frost, J. M.; Terban, M. W.; Zhai, H.; Alatas, A.; Owen, J. S.; Walsh, A.; Billinge, S. J. L. *ArXiv:1606.09267* **2016**, 1−10.

(96) Zheng, F.; Tan, L. Z.; Liu, S.; Rappe, A. M. *Nano Lett.* **2015**, *15*, 7794−7800.

(97) Azarhoosh, P.; McKechnie, S.; Frost, J. M.; Walsh, A.; van Schilfgaarde, M. *APL Mater.* **2016**, *4*, 091501.

(98) Delaire, O.; Ma, J.; Marty, K.; May, A. F.; McGuire, M. A.; Du, M.-H.; Singh, D. J.; Podlesnyak, A.; Ehlers, G.; Lumsden, M. D.; Sales, B. C. *Nat. Mater.* **2011**, *10*, 614−619.

(99) Shiga, T.; Shiomi, J.; Ma, J.; Delaire, O.; Radzynski, T.; Lusakowski, A.; Esfarjani, K.; Chen, G. *Phys. Rev. B: Condens. Matter Mater. Phys.* **2012**, *85*, 1−5.

(100) Lee, S.; Esfarjani, K.; Luo, T.; Zhou, J.; Tian, Z.; Chen, G. *Nat. Commun.* **2014**, *5*, 3525.

(101) Pisoni, A.; Jaćimović, J.; Barišić, O. S.; Spina, M.; Gaál, R.; Forró, L.; Horváth, E. *J. Phys. Chem. Lett.* **2014**, *5*, 2488−2492.

(102) Mori, M.; Saito, H. *J. Phys. C: Solid State Phys.* **1986**, *19*, 2391.

(103) Kuok, M. H.; Saw, E. L.; Yap, C. T. *Phys. Status Solidi* **1992**, *132*, K89−K92.

(104) Zheng, J.-C.; Huan, C. H. A.; Wee, A. T. S.; Kuok, M. H. *Surf. Interface Anal.* **1999**, *28*, 81−83.

(105) Scaife, D. E.; Weller, P. F.; Fisher, W. G. *J. Solid State Chem.* **1974**, *9*, 308−314.

(106) Glazer, A. M. *Acta Crystallogr., Sect. B: Struct. Crystallogr. Cryst. Chem.* **1972**, *28*, 3384−3392.

(107) Brown, I. D. *Chem. Soc. Rev.* **1978**, *7*, 359−376.

(108) Brown, I. D. *Chem. Rev.* **2009**, *109*, 6858−6919.

(109) Brese, N. E.; O'Keeffe, M. *Acta Crystallogr., Sect. B: Struct. Sci.* **1991**, *47*, 192−197.

(110) Young, J.; Rondinelli, J. M. *J. Phys. Chem. Lett.* **2016**, *7*, 918−922.

(111) Smith, E. H.; Benedek, N. A.; Fennie, C. J. *Inorg. Chem.* **2015**, *54*, 8536−8543.

(112) Berastegui, P.; Hull, S.; Eriksson, S. *J. Phys.: Condens. Matter* **2001**, *13*, 5077−5088.